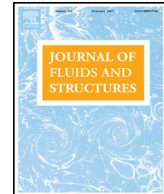




Contents lists available at ScienceDirect

Journal of Fluids and Structures

journal homepage: www.elsevier.com/locate/jfs



Experimental analysis of a strong fluid–structure interaction on a soft membrane—Application to the flapping of a yacht downwind sail

Julien Deparday ^{a,*}, Benoit Augier ^b, Patrick Bot ^c

^a UNFoLD, Institute of Mechanical Engineering, Ecole Polytechnique Fédérale de Lausanne, CH-1015 Lausanne, Switzerland

^b IFREMER, Marine Structures Laboratory, Z.I. Pointe du Diable, CS 10070, 29280 Plouzané, France

^c Naval Academy Research Institute - IRENAV CC600, 29240 BREST Cedex 9, France



HIGHLIGHTS

- In-situ time resolved measurements on a thin flexible membrane inflated by the wind.
- Study of a flapping instability of the weakly constrained free leading edge.
- Peak of load and creation of large suction when membrane recovers its full shape.
- Dynamics of flapping well characterized by two bi-orthogonal decomposition modes.
- Flapping mechanism has a constant reduced frequency.
- Proposed physical mechanism is based on creation and shedding of Leading Edge Vortex.

ARTICLE INFO

Article history:

Received 31 October 2017

Received in revised form 26 April 2018

Accepted 6 June 2018

Keywords:

Fluid–structure interaction

Full-scale experiment

Modal decomposition

Pressure measurements

Soft membrane

ABSTRACT

In the present study we investigate the flapping instability of a light, soft, highly cambered membrane subject to wind loading. An original in-situ experiment is developed where time-resolved pressures and forces are measured on a full-scale yacht downwind sail called a spinnaker. Particular features of this aero-elastic problem are that the membrane is weakly constrained – held only at three corners –, has a free leading edge, and has no proper shape in the absence of wind loading. In usual operating conditions, the soft structure is subject to a flapping instability giving rise to almost periodic folding and unfolding of the fore part of the sail, associated to strong variations of pressures and forces. This dynamic behavior is analyzed in detail and the space-time evolution of pressures on the membrane is linked to the flapping phenomenon. A peak in forces is observed when the membrane recovers its full shape. Thanks to the Bi-Orthogonal Decomposition (BOD) applied to the pressure fields, the dynamic behavior is reasonably well represented by the two first modes where mode 1 mostly carries the global aerodynamic force behavior and mode 2 mostly represents the effects of the membrane flapping. A physical mechanism of the flapping process is proposed based on the discussion of aerodynamic pressures and strains in the membrane.

© 2018 Published by Elsevier Ltd.

* Corresponding author.

E-mail address: julien.deparday@epfl.ch (J. Deparday).

Abbreviations and notations

MAV	Micro Air Vehicle
BOD	Bi Orthogonal Decomposition
POD	Proper Orthogonal Decomposition
C_{fill}	Surface elastic modulus in the fill of the spinnaker material (57 kN/m)
C_{warp}	Surface elastic modulus in the warp of the spinnaker material (83 kN/m)
E	Elastic modulus (N/m ²)
EI	Flexural rigidity (N m ²)
F_{aero}	Aerodynamic force (N)
f_r	Reduced frequency ($\frac{f_r L}{U_0}$)
L	Characteristic length of spinnaker ($\sqrt{S} = 8.25$ m)
M	Mass number ($\frac{\rho_s U_0^2 L}{\rho_f L}$)
Re	Reynolds number ($\frac{\rho_f U_0 L}{\mu}$)
S	Spinnaker area (68 m ²)
th	Average thickness of the spinnaker (5.0×10^{-5} m)
U_0	Characteristic fluid velocity (m/s)
$\mathbf{U}(\mathbf{x}, t)$	Spatio-temporal signal
V_∞	Onset flow velocity: Apparent Wind Speed for the yacht (m/s)
w	Normal displacement from plane ($\underline{u}, \underline{v}$) (m)
α_k	BOD eigenvalue
ΔC_P	Differential pressure coefficient ($\frac{P_{leeward} - P_{windward}}{\frac{1}{2} \rho_f V_\infty^2}$)
Δp	Differential pressure (Pa)
$\underline{\underline{\kappa}}$	Curvature tensor (m ⁻¹)
κ_u	Curvature in u direction (m ⁻¹)
κ_v	Curvature in v direction (m ⁻¹)
μ	Dynamic viscosity of the fluid (1.80×10^{-5} Pa s)
Π_1	Effective stiffness ($\frac{EI}{\rho_s U_0^2 L^3}$)
ρ_f	Density of air (1.23 kg/m ³)
ρ_s	Density of the solid (kg/m ³)
$\underline{\underline{\sigma}}$	Stress tensor in the fluid (N/m ²)
$\varphi_k(x)$	BOD spatial modes (<i>topos</i>)
$\psi_k(t)$	BOD temporal modes (<i>chronos</i>)

1. Introduction

It is now well understood that Fluid–Structure Interaction (FSI) is a key feature to fully understand the mechanisms leading to optimized performance of flexible structure in a flow (Daniel and Combes, 2002). Bio-inspired or biomimetic concepts have led to the study and optimization of propulsion systems designed by evolution in the aerodynamics of birds and insects (Combes and Daniel, 2001; Mountcastle and Daniel, 2009; Michelin and Llewellyn Smith, 2009b) (see Shyy et al., 2010 for a large review on insect flight) and the hydrodynamics of fishes (Fish, 1999; Leroyer and Visonneau, 2005). These optimized hydrodynamic systems have raised questions on the link between the Strouhal number, the wake patterns and the propulsion efficiency (Schouwiler et al., 2005; Bergmann and Iollo, 2011) and the benefit of flexibility in the structure for a certain range of Strouhal number (Miao and Ho, 2006; Heathcote et al., 2008; Michelin and Llewellyn Smith, 2009b; Murua et al., 2010; Marais et al., 2012). Recent examples of design with optimized structure, wing or fin shape and motion have contributed to the development of Micro Air Vehicle (MAV) (Wood, 2007; Takizawa et al., 2012, 2014) or hydrodynamic propulsion system (Augier et al., 2014b; Yan et al., 2015).

It is well known that even in steady conditions, instabilities can lead to a dynamic response of the flow or a fluid–structure system, well described at low Reynolds number with a cylinder obstacle (Williamson, 1996; Khalak and Williamson, 1996, 1999). These instabilities can have a significant impact on the structure as for example the flapping flag instability (Alben, 2008; Eloy et al., 2011), the flutter of parallel flexible plates (Schouwiler and Eloy, 2009) or of a ribbon hanging in axial flow (Lemaître et al., 2005). This flapping motion of flexible plates placed in a parallel flow has been subject of numerous experimental (Huang, 1995; Watanabe et al., 2002; Bleischwitz et al., 2017; Zhang et al., 2017), theoretical (see Paidoussis, 2004 for a review) and numerical studies (Zhu and Peskin, 2002; Connell and Yue, 2007; Alben, 2008). Michelin and Llewellyn Smith (2009a) describe the flapping motion as the result of the fluttering instability of the flexible structure's position under the competing effects of solid inertia, aerodynamic pressure forcing and solid flexural rigidity. In some cases, structure deformation can be linked to the leading edge vortex, tip vortices and vibrations to the harmonics of wake instabilities

Table 1

Main non-dimensional numbers describing the fluid–structure interaction on the asymmetric spinnaker, and comparisons with other fluid–structure interaction mechanisms. Non dimensional numbers for MAV and Flag are taken respectively from Rojratsirikul et al. (2011) and Connell and Yue (2007).

Field of research		Spinnaker	MAV	Flag
Characteristic non-dimensional numbers				
Effective stiffness	$\Pi_1 = \frac{EI}{\rho_s U_0^2 L^3}$	1×10^{-9}	7×10^{-5}	1×10^{-4}
Reynolds number	$Re = \frac{\rho_f U_0 L}{\mu}$	3×10^6	3×10^4	1×10^3
Mass number	$M = \frac{\rho_s th}{\rho_f L}$	5×10^{-3}	1×10^2	$2 \times 10^{-2} \rightarrow 3 \times 10^{-1}$
Reduced frequency	$f_R = \frac{f_L}{U_0}$	0.8	$0.5 \rightarrow 1.1$	0.7

(Rojratsirikul et al., 2011). When the structure is very flexible such as a membrane, large deformations are expected and the fluid–structure coupling may be strong, particularly if the membrane is not highly constrained (Glück et al., 2001; Knight et al., 2010; Durand et al., 2014; Michalski et al., 2015; Deparday et al., 2016; Chae et al., 2016; Tiomkin and Raveh, 2017; Waldman and Breuer, 2017).

In this paper, we present the investigation of a soft and light membrane inflated by the wind which is subject to a flapping instability. To this end, we study an offwind yacht sail called an asymmetric spinnaker at full scale in real sailing conditions. The spinnaker is a low-aspect-ratio highly-curved, very light and flexible structure held only at three corners. This rather unconstrained structure has no proper shape in the absence of wind loading and the geometry may change drastically according to the wind and the sail adjustments. Spinnakers are subject to the so-called flapping instability, even in steady condition. This flapping corresponds to a folding oscillation of the leading edge of the sail and is commonly associated to the best aerodynamic performance trimming. The benefit of the flapping has been recently measured during a wind tunnel campaign (Aubin et al., 2017, 2018). Even if the flapping instability may look similar to previously cited literature, it is of different nature: high Reynolds number (10^5 – 10^6) of the flow, highly cambered 3D structure only held by 3 points with a free leading edge, 3D flow structure due to the atmospheric wind gradient and low aspect ratio of a 3D geometry, fluid added mass up to 100 times the structural mass, dynamic behavior inherent to sailing yacht.

Table 1 sums up the quantities defining the flapping phenomenon of a spinnaker sail. The Reynolds number is higher than for MAV or flag cases, the effective stiffness is lower meaning a more flexible structure, and also lighter with a lower mass number compared to other cases.

The dynamic behavior can be caused by the surrounding environment (the sea state and the wind), but can also be caused by the action of the crew while trimming. Literature has pointed out the difficulty of considering the realistic sailing environment of a yacht (Marchaj, 1962; Garrett, 1987). Wind tunnel is commonly used to control the aerodynamic and motion environment of yacht. It has been subject to a large number of experimental studies to measure both the aerodynamic loads on the boat frame using a balance (Flay, 1996; Viola and Flay, 2009; Fossati and Muggiasca, 2011; Campbell, 2014) and the pressure and 3D shape deformation of the structure (Graf and Müller, 2009; Viola and Flay, 2011; Viola et al., 2013). Recent studies have highlighted the non-trivial effect of dynamic oscillation on the aerodynamic forces (Gerhardt et al., 2011; Fossati and Muggiasca, 2011; Augier et al., 2013, 2014a). Nevertheless, wind tunnel testing violates some rules of similitudes as Reynolds number, the ratio of fabric weight or membrane stress to wind pressure (Flay, 1996) and cannot reproduce properly all the physical phenomena present at full-scale. Hence, full-scale experiments in real sailing conditions are necessary to investigate the real-world application.

Despite the hostile environment for instrumentation, the multi-physics involved and the number of quantities to measure, full-scale experiment on sailing yacht is then an interesting approach to fully respect the similitude necessary to properly investigate this Fluid–Structure problem. In this paper, we focus on the description of the flapping instability observed at full scale on a spinnaker. First, the flow and structure specificities of the system are detailed, and the original experimental set up on the instrumented yacht is presented. After describing the overall behavior of the spinnaker, pressure distributions and forces are then presented for a flapping session and analyzed through a BOD (Bi Orthogonal Decomposition) approach. Time and space pressure evolutions are extracted and studied. From the conclusions drawn, a physical mechanism is proposed to explain the flapping instability.

2. System apparatus

Full-scale tests are performed with an instrumented yacht developed at the Research Institute of the Naval Academy (IRENav). Instrumentation on yachts has been subject to different projects and approaches in terms of measurement systems.

Sail boat dynamometers have been developed to measure forces from sails transmitted to the boat frame (Herman, 1989; Hochkirch and Brandt, 1999; Masuyama, 2014) and more recently Fossati et al. (2015). In this configuration, the whole rig is connected to a rigid frame acting as an aerodynamic balance. The global aerodynamic forces are expressed at the center of the balance. Another configuration is to measure the forces separately in the rigging line as developed by Augier et al. (2012) in upwind condition and Deparday et al. (2014) for downwind condition with spinnakers. External load sensors can be coupled to other sensors in order to measure the sail shapes with camera recognition (Augier et al., 2012, 2013), the forces

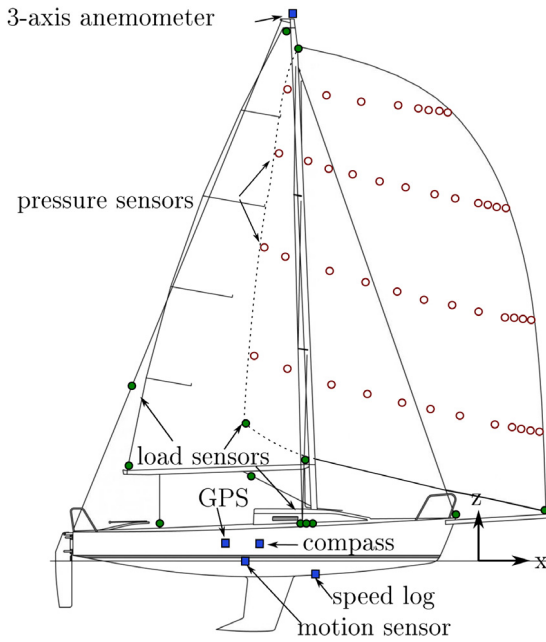


Fig. 1. General arrangement of the experimental set-up on the J/80. 16 load sensors (green discs), 44 pressure taps (red circles), and wind and boat sensors (blue squares).

and the directions on the three corners of spinnakers (Le Pelley et al., 2015), pressures on sails for upwind and downwind sails (Viola and Flay, 2010; Le Pelley et al., 2012; Lozej et al., 2012; Motta et al., 2014; Deparday et al., 2014).

In the present study, an instrumented J/80 class sailing yacht, an 8-m one-design cruiser racer is used. Boat data and wind data, loads on the standing rigging and on the sails are recorded. More details on the instrumentation can be found in Augier et al. (2012) and Deparday (2016). Pressure sensors, developed by the Yacht Research Unit at the University of Auckland (Le Pelley et al., 2012) are stuck on the spinnaker to acquire the dynamic pressure distribution. All data acquisition is resolved in time. Fig. 1 shows the arrangement of all the sensors set onboard.

2.1. Spinnaker

Fig. 2 presents the main terminology for a spinnaker. A spinnaker is held by 3 points that are called head, tack and clew. The sail area is $S = 68 \text{ m}^2$. The 12-m long curved leading edge is 1 m longer than the distance between the two points holding the leading edge (head and tack points). As the 3D shape of the sail is far from the extrusion of a 2D-section, with a sheared and twisted onset flow, the characteristic length is defined as the square root of the sail area, i.e. $L = 8.25 \text{ m}$. It is also close to the curved length of the membrane at mid-height.

The spinnaker is made of Nylon panels assembled by gluing and/or sewing on their curved edges, generating camber and therefore a non-developable surface. Nylon panels are considered as an orthotropic material with warp and fill ($C_{\text{warp}} = 83\,000 \text{ N/m}$ and $C_{\text{fill}} = 57\,000 \text{ N/m}$). The fabric thickness is measured at $th = 0.05 \text{ mm}$. Average Elastic modulus is $E = 1.5 \text{ GPa}$. Its surface density is measured at $\rho_{\text{surf}} = 0.05 \text{ kg/m}^2$. Due to its small thickness compared to the other dimensions and its lightness, the sail can be considered as a membrane with no flexural rigidity.

2.2. Pressure measurement

On the spinnaker, 44 low-range differential pressure sensors are located on the surface along 4 horizontal stripes: at 1/4, 1/2, 3/4 and 7/8 height of the spinnaker from the foot (see Fig. 1). Twelve pressure transducers are used on each of the first 3 stripes and 8 for the top one. There is a higher concentration of pressure taps near the leading edge to be able to record high gradients in this area and potential leading-edge suction peaks. The space resolution in the spanwise direction is rather limited, but low pressure gradients are expected in this direction. These sensors measure a difference of pressure between the suction side and the pressure side using the piezoresistive effect. Reference pressure is not needed in this configuration. The sensors are stuck on one side and are positioned facing 2 mm-diameter holes in the sail to measure the pressure jump across the sail. The whole pressure system (pressure taps, wiring, A/D converters, data multiplexers and emitting systems) adds a total mass of around 2 kg, which is significant on a 4.5 kg sail. The sail shape may be affected for low wind speeds where the sail may not fly properly, but in the wind speed range of the present results, forces on the sail corners are of the

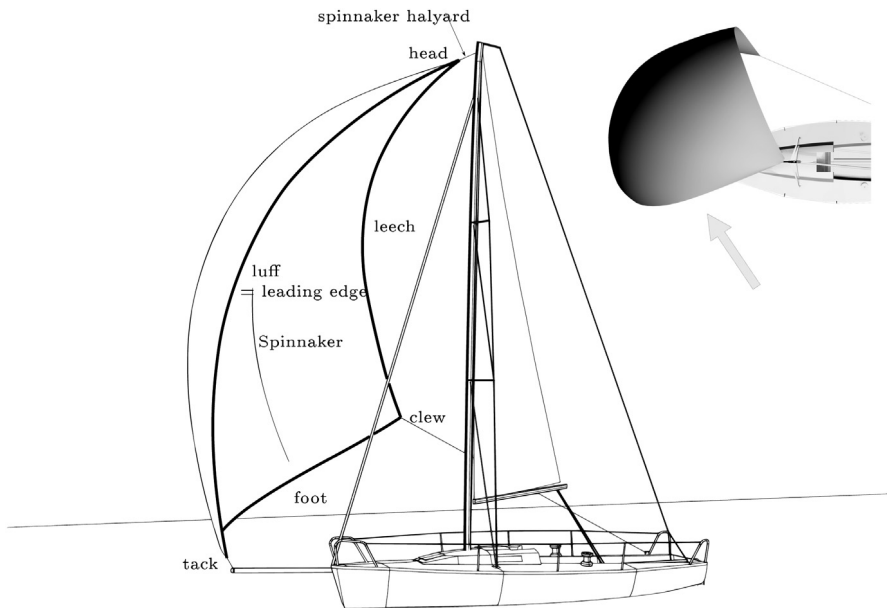


Fig. 2. Our case of study: a spinnaker sail. A thin and flexible surface held at 3 points with a free leading edge. Upper right corner: bird's eye view, the arrow shows the direction of the onset flow (apparent wind).

order of 10^3 N and the extra mass has no effect on the sail shape. The sail stiffness is locally increased by the cloth patches covering the taps and the wires, but remains small enough compared to the flow dynamic pressure (see Table 1).

These pressure transducers are synchronized with the other data. The pressure sensors dynamics is around 3 kHz, and the sampling frequency is approximately 10 Hz which is 15 times larger than the observed frequency of the flapping instability. The maximum pressure range is ± 1 kPa with a resolution of 0.5 Pa. The system had a calibration procedure to minimize deviation and error. Occasional strong accelerations may bias the pressure measurement because of the sensing piezoresistive membrane inertia which would be added to the air added mass effect for strong accelerations. But the air added mass is dominant (see Table 1). Anyway, the description of pressures will mostly be qualitative in this article. The pressure acquisition system is further described in Motta et al. (2014).

2.3. Load measurement

The corners of the spinnaker (head, tack and clew) are equipped with instrumented shackles. Due to the high displacements of the spinnaker (in the order of magnitude of 1 to 5 m for the spinnaker used in these experiments), these instrumented shackles communicate wirelessly to the acquisition system transmitting data at a sampling frequency of 25 Hz to the receiver inside the boat. The delay between the transmission and reception of data is insignificant compared to the time scales of the dynamics in sailing.

The measurement errors are less than 2% of the measurement range (5000 N).

2.4. Wind measurement

The spinnaker sail is used for a wide range of wind angles and speeds. Therefore, its shape and its aerodynamic loads vary widely with the wind (Motta et al., 2014; Deparday et al., 2016). The flow seen by the sails (called Apparent Wind) is the vector sum of the wind (called True Wind) and the opposite yacht velocity. Due to the vertical wind gradient in the atmospheric boundary layer, the Apparent Wind on the sails is sheared and twisted along the vertical direction.

The apparent wind is measured at 10 Hz by a 3-axis ultrasonic anemometer located 1 m above the masthead – 1.6 m above the spinnaker head –, which is typical of a yacht in racing conditions. Note that the sail angle of attack varies along the span and cannot be easily determined. It is affected by the Apparent Wind Angle (angle between the Apparent Wind and the yacht axis), by the trimming of the sail thanks to the line (sheet) attached to the rear bottom corner (clew, see Fig. 2), and by the deformation of the sail under fluid loading. Hence, only the measured apparent wind angle is considered in this article and will be called “wind angle”.

2.5. Definition of “stable” periods

Sea trials were performed in the sheltered bay of Brest, France, offshore Ecole Navale. During these experiments, the weather conditions were rather stable and the sea was flat. For each run, the sheet length is adjusted to trim the sail on the

verge of luffing and kept constant during the run, while the helmsman drives the yacht to keep the apparent wind angle as constant as possible.

In the real world, wind variations cannot be controlled. As we are interested in the intrinsic dynamics of the aeroelastic system and not in its response to wind variations, the data presented here is analyzed only on runs where the standard deviation is below 4° for the wind angle and below 10% of the average wind speed for the wind speed. These thresholds revealed good trade-offs to get a significant number of runs with stable conditions as inputs to the FSI system. Each stable period is processed individually, and around 30 runs were recorded in a large range of wind angles between 55° and 140°.

The sail shape was measured during other experimental campaigns in the same conditions thanks to photogrammetry, as described in Deparday et al. 2016, where a detailed analysis of the sail shape is made for different sailing conditions (wind angle particularly). In the present work, the focus is on the dynamics of pressures and the previously measured sail shapes are only used to draw the pressure spatial patterns (see Fig. 8).

3. Specific behavior of a spinnaker

Before describing the flapping behavior using the measurements of pressures, sail shape and loads, the general behavior of the sail is presented, as the shape changes considerably according to the wind angle and trimming.

3.1. Spinnaker general behavior

A salient feature of the spinnaker aeroelastic problem is that the membrane has no proper shape in the absence of fluid loading. When the wind angle is in a certain range (between 50° and 140°), and the sail properly trimmed, the spinnaker is inflated and has a given shape.

For a given wind angle, if the sail is adjusted with a short enough sheet length, it is then inflated and has a constant shape (see Fig. 3(a)). This case is usually called over-trimmed as it is not optimum in terms of performance. When the clew sheet is eased, the sail shape changes towards more camber and lower angle of attack until the leading edge starts flapping periodically (see Fig. 3(b)). Note that the forward membrane side (the luff) is free and rounded (see Fig. 2). If the sheet is eased more, the flapping area extends downstream (see Fig. 3(c)) until the sail collapses (see Fig. 3(d)).

In practice, high performance sailors permanently adjust the sheet length in order to maintain the sail leading edge on the verge of luffing and avoid collapse. In this work, we investigate sustained flapping situations with a fixed sheet length in order to study the intrinsic unsteadiness of the aeroelastic system due to the flapping instability.

3.2. Description of the flapping

The following description of the flapping is based on numerous measurements identified as stable periods (according to Section 2.5) where flapping of the leading edge occurs more or less periodically while the sail adjustment was fixed. One representative run is shown on Fig. 4 as an example.

Fig. 4 presents space-time diagrams of $\Delta C_p(x, t)$ (a) and (b) at stripes 3/4 and 1/2 height of the sail where flappings of the spinnaker occur. White lines highlight the zero differential pressure. The time series of the force coefficients on the three corners (head, tack and clew) is represented in Fig. 4(c). Curly braces indicate when the spinnaker is seen folded. Positive differential pressure – i.e. pressure larger on the suction side than on the low pressure side – appears when the spinnaker is folded resulting in flipped sides. A representative flapping period is chosen between 67.5 s and 69 s and decomposed in 4 instants A, B, C and D for a deeper analysis.

To describe this flapping, the 4 instants are chosen during this periodic behavior, every 0.4 s. Fig. 5 presents the recorded shape of the leading edge at these 4 instants.

Instant A : Just at the beginning of folding, loads at the corners of the sail are at a minimum.

$A \rightarrow B$: The folding starts with an increase of the differential pressure at the leading edge going positive. The maximum of pressure is reached at the leading edge for the 3/4 stripe. Nonetheless, loads are increasing.

Instant B : The leading edge is still folding at the 1/2 stripe. During the unfolding at the 3/4 stripe, a suction occurs at 10% of this stripe.

$B \rightarrow C$: The suction is propagating upstream and downstream at the 3/4 stripe. Folding is propagating from the top of the sail to the 1/2 stripe.

Instant C : The leading edge is folded at its maximum at 1/2 stripe. After this instant, the leading edge starts unfolding. Loads keep increasing.

$C \rightarrow D$: The suction zone is appearing at the 1/2 stripe and is propagating upstream and downstream and keeps propagating on the higher part of the sail.

Instant D : Just after the leading edge is completely unfolded. Loads on the corners of the sail are at a maximum. Just after this peak, the suction zone disappears on both stripes and the loads drop down to values measured at instant A.



Fig. 3. Various shapes of the sail for different clew sheet length (trimming).

The flapping is a 3D instability as illustrated by the different dynamics observed at 3/4 and 1/2 of the span. Folding wave and pressure peaks propagate in both chordwise and vertical direction.

As illustrated in Fig. 4, the pressure evolution in space and time at the 3/4 height stripe is similar to the 1/2 height stripe with a creation of the high suction area at the leading edge when it is completely folded. This suction area is increasing during the unfolding stage. However, at 3/4 height, when the section has recovered its full shape, the high suction area stays at the leading edge. It disappears when the high suction at 1/2 stripe vanishes. This is why the highest absolute differential pressure, hence the loads on the corners, are observed at instant D.

This description of this specific dynamics of a spinnaker is based on representative periods where leading edge flapping occurs. The run exemplified here is a typical pattern which is spotted in the other measurements carried out at different wind angles, and was also observed on a larger spinnaker (Motta et al., 2015). To detect these patterns in the other measurements and analyze them automatically, we used the Bi-Orthogonal Decomposition method. It is therefore possible to characterize the spatial patterns of pressure variations, in order to decompose complex pressure evolutions into simpler modes. These

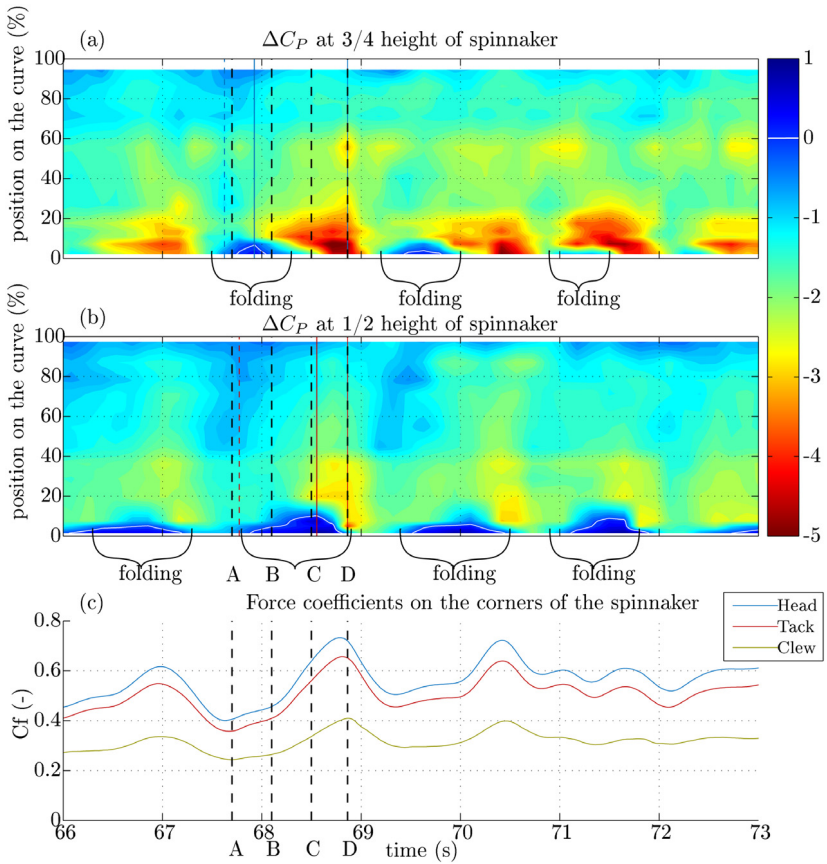


Fig. 4. Evolution of the pressure distributions and loads on spinnaker. Space–time diagrams of $\Delta C_P(x, t)$ at 3/4 height (a), at 1/2 height (b); time series of load coefficients measured on the sail corners (c).

pressure modes can help to describe a global temporal behavior in a better way than analyzing each pressure sensor signal, which is more local and noisier. They can also be correlated with other recorded data.

4. Breakdown of the flapping phenomenon into modes

4.1. Bi-Orthogonal Decomposition

The Bi-Orthogonal Decomposition (BOD) breaks a space–time signal down into spatial modes, called *topos* $\varphi_k(\mathbf{x})$ (with $\varphi_k \in \mathbf{L}^2(\mathbf{X})$) and temporal modes, called *chronos* $\psi_k(t)$ (with $\psi_k \in \mathbf{L}^2(\mathbf{T})$). It has first been introduced by Aubry et al. (1991). The exhaustive demonstration can be found in this paper. Hénon and Santi (2003) demonstrated this method is well adapted for fluid–structure interaction problems. The BOD of the input data $U(x, t)$ (in our case $U(x, t) = \Delta C_P(x, t)$ function of space $\mathbf{x} \in \mathfrak{N}^2$ and time $t \in \mathfrak{N}$, with $U(\mathbf{x}, t) \in L^2(\mathbf{X} \times T)$, $\mathbf{X} \subset \mathfrak{N}^2$ and $T \subset \mathfrak{N}$) is written as:

$$\mathbf{U}(\mathbf{x}, t) = \sum_{k=1}^{\infty} \alpha_k \psi_k(t) \varphi_k(\mathbf{x}). \quad (1)$$

The set of the eigenvalues $\lambda_k = \alpha_k^2$ associated to either the topos or the chronos are the eigenmodes of the respectively spatial and temporal correlation operators. Since the eigenvalues are identical for chronos and topos, these latter are intrinsically coupled.

The BOD is a deterministic tool rather than statistical and the signals to be decomposed need to be only square integrable and not necessarily ergodic and stationary as required for the Proper Orthogonal Decomposition (POD). But similarly to the POD, the sum of the BOD eigenvalues $\lambda_k = \alpha_k^2$ is equal to the global energy of the signal. Furthermore, the BOD theorem

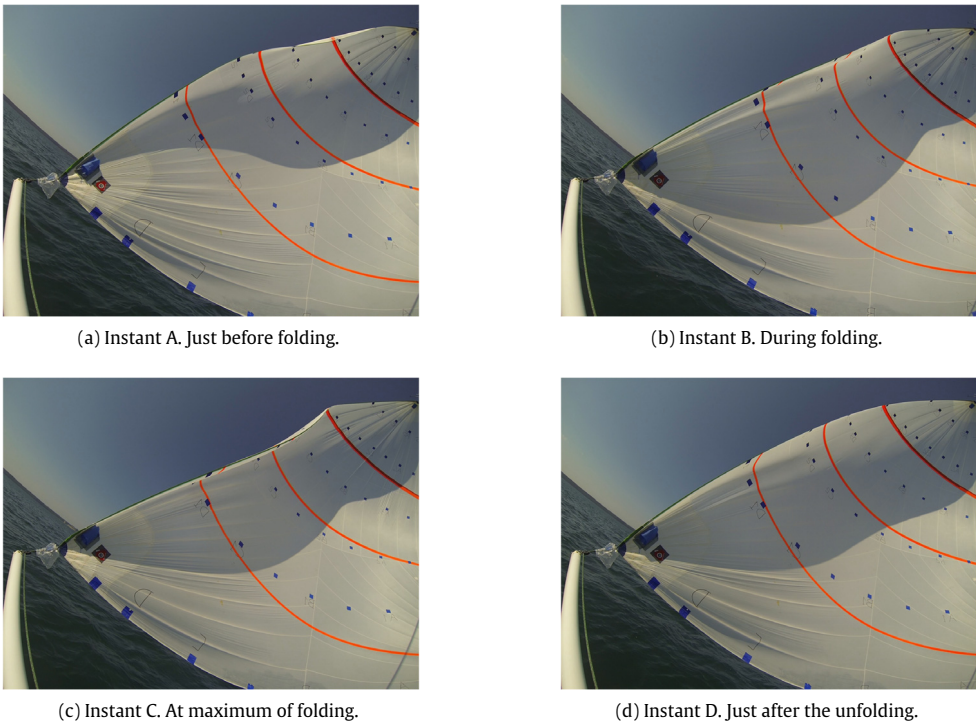


Fig. 5. Snapshots of the flying shape during flapping at the four selected times. Onboard pictures taken from the deck looking up.

proves that [Aubry et al. \(1991\)](#):

$$\begin{aligned} \alpha_1 &\geq \alpha_2 \geq \dots \geq 0, \\ \lim_{M \rightarrow \infty} \alpha_M &= 0, \\ \langle \varphi_k, \varphi_l \rangle &= \overline{\psi_k \psi_l} = \delta_{k,l}. \end{aligned} \tag{2}$$

However, in the BOD, the temporal or spatial mean should be kept and not removed as it is commonly done before applying the POD (see [Hémon and Santi, 2003](#)). It is particularly important when there is a strong heterogeneity of the mean components, as in the present case with high periodic variations for multiple pressure signals.

4.2. Main BOD results

In the following part, out of 30 stable runs recorded with a fixed trimming, the analysis is made on 16 runs lasting 20 s minimum, identified as stable enough sustained flapping situations. It turns out that all observed behaviors could be classified in two categories with different behaviors: *small wind angle* (angle lower than 100°) and *large wind angle* (angle larger than 100°), with all results in each category being similar. Then, the examples of large and small wind angles shown in [Figs. 8 and 9](#) are representative of the whole dataset.

The average sail shape, pressure distribution and loads are significantly different between small and large angles (see [Fig. 8](#) and also [Motta et al., 2015](#); [Deparday et al., 2016](#); [Deparday, 2016](#)). For large angles, the flow is mainly detached around the sail, the apparent wind speed lower hence the aerodynamic loads smaller. Furthermore, the flapping phenomenon does not appear at the same height of the span at these 2 extreme wind angles: while for low wind angle (about 70°), the main folding area is the leading edge at the middle of the span (see [Section 3.2](#)), for large wind angles (about 120°) the top (3/4 of the span) of the leading edge folds.

4.2.1. Eigenvalues

[Fig. 6](#) shows the computed eigenvalues of the BOD for all stable data computed. Mode 1 is clearly predominant containing about 50% of the energy of the pressure signal. Mode 2 is at about 10%. Mode 3 and 4 are between 3 and 5% and further modes less than 3%. In [Fig. 6](#), computed eigenvalues for large wind angles plotted in red are slightly higher for larger modes as the apparent wind speed is lower and therefore the pressure fluctuations are a bit noisier. It means higher modes have slightly more energy. Nonetheless, the general trend is similar for all wind angles especially in the first 3 modes.

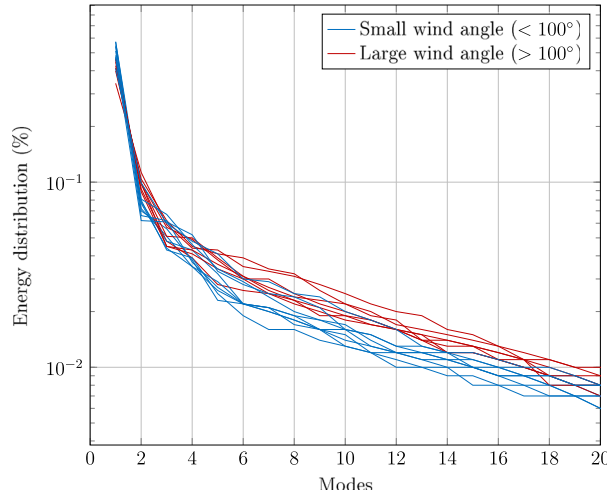


Fig. 6. Eigenvalues for each pressure mode for all computed “stable” periods. They represent the energy contained in each BOD mode.

[Fig. 7](#) shows an example of the original pressure signal for the half stripe and its reconstruction with mode 1 only, with modes 1 and 2, and with the 4 first modes. It is shown that the reconstructed signal with modes 1 and 2 fits the original signal quite well, and that the addition of modes 3 and 4 does not bring much more information to the understanding of the dynamics, but only minor refinements.

It is visible in [Fig. 7](#) that the global (temporal) fluctuations of pressures are mainly contained in mode 1, and mode 2 mainly holds more local fluctuations associated with the flapping: see sharp variations near the leading edge which are resolved only when mode 2 is added. Mode 1 displays the high suction area and the addition of mode 2 enables to represent the suction propagation described in [Section 3.2](#).

4.2.2. Topos

[Fig. 8](#) presents the topos of the first 4 modes for the two characteristic wind angles. Topos absolute values are arbitrary as they have to be combined with the chronos and the eigenvalues to build the pressure evolution (see Eq. (1)). Nonetheless, variation of topos are relevant to spot pressure patterns.

The mode 1 topos presents a high value at the leading edge close to the folding area. The topos value decreases progressively along the chord. The mode 2 topos has a characteristic opposition of 2 zones of high and low value at the leading edge. Low value zone of mode 2 indicates where the folding appears. The high value zone of mode 2 corresponds to the maximum topos values of mode 1 which is where the high suction occurs. The first 2 modes of the small wind angle are consistent with the pressure and load evolution presented in [Fig. 4](#): folded area at mid-span and high suction at 3/4 height of the sail.

The first two modes have similar topos for all wind angles, while a tendency is not clear on higher modes as seen in [Fig. 8](#). Moreover, rather high level of noise in these real-world experiments and the limited space resolution in the spanwise direction make interpretation of higher modes a bit difficult. Then, the analysis is focused on the first two modes which prove to represent well the dynamic behavior of the flapping phenomenon on pressures, as shown on [Fig. 7](#), even if there is no sharp drop in the eigenvalues. The spatial average topos value of mode 2 is around zero (positive and negative topos values at the leading edge cancel out, and values are close to zero anywhere else on the sail). Therefore, for mode 2, due to its low eigenvalues and average topos value around zero, the aerodynamic load associated to mode 2 is marginal.

4.2.3. Chronos

[Fig. 9](#) presents the chronos of the first 2 modes for the two characteristic wind angles.

Chronos of mode 1 are approximately at the same value ($2 \cdot 10^{-2}$) for small and large wind angles, whatever the spinnaker shape. Hence, since the eigenvalue and the spatial average of the topos for mode 1 have also similar values for small and large wind angles, the aerodynamic load coefficient generated by mode 1 remains approximately constant for all wind angles.

As illustrated in [Fig. 9](#), mode 2 shows coherent oscillations corresponding to flapping events with a pseudo periodic behavior. The characteristic frequency is determined as the inverse of the pseudo-periods detected in the mode 2 chronos for all studied stable periods. [Fig. 10](#) shows the average value and scatter for each wind angle measured. Results are plotted as the reduced frequency f_r :

$$f_r = \frac{f_s \sqrt{S}}{V_\infty} \quad (3)$$

with V_∞ corresponding to the average wind speed measured for the “stable” period at the considered wind angle.

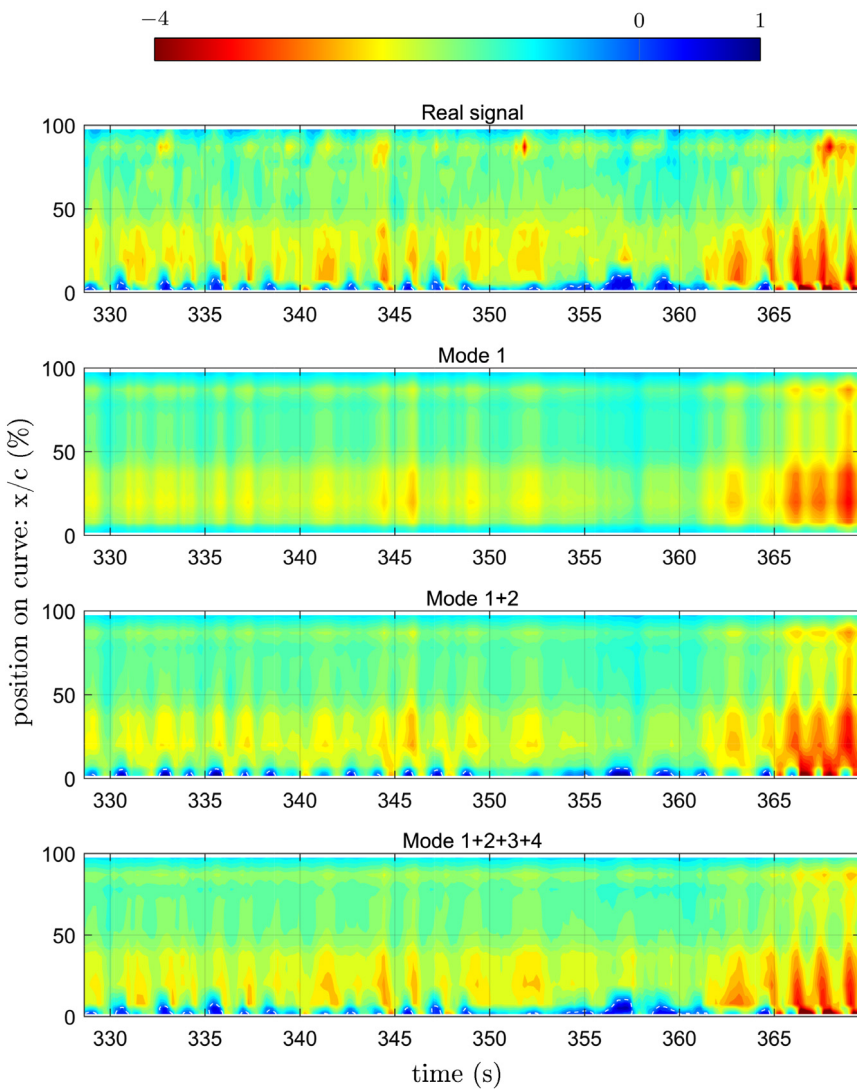


Fig. 7. Space–time reconstruction of pressure for the half stripe for a small wind angle (50°).

A fairly constant reduced frequency is observed in Fig. 10, illustrating a linear dependence of the pseudo-frequency with the wind speed. It suggests that the dynamics of the sail's flapping, is mostly driven by aerodynamic phenomena. These aerodynamic phenomena could be a lock-in due to the shedding of the leading edge vortex, or the dynamics of the trailing edge vortex shedding as the flow is mostly detached on a large part at the trailing edge. The three dimensional aspect of the flow could play a role too.

In conclusion, most of the aerodynamic force is contained in mode 1. Indeed, even if temporal fluctuations of mode 2 look large (see Fig. 9), as $\lambda_2 \ll \lambda_1$ and the space-average of mode 2 topos is very small (Section 4.2.2), the amplitudes of aerodynamic force associated with mode 1 are one order of magnitude higher than those associated with mode 2. The signature of flappings is also visible in mode 1 chronos, adding fluctuations to the global aerodynamic force. Mode 2 does not contribute significantly to the aerodynamic force but the structural dynamics of the flapping is highlighted by the mode 2 chronos, where the flapping frequency is determined from the time-scale of the coherent oscillations. The same frequency can be detected in the signals of corner loads, but the latter are much more perturbed by variations in the environmental conditions. The flapping frequency varies linearly with the wind speed.

The breakdown of the flapping phenomenon into BOD modes makes it possible to separate the dynamic load generated by the sail, mostly seen in mode 1, and the structural dynamic shape of the sail highlighted by mode 2. Mode 1 could then be seen as the *aerodynamic mode* and mode 2 as the *structural mode*. The combination of the 2 modes contributes to the propagation of the flapping instability. This simplified description represents a simplified general vision of the flapping phenomenon, when the reality is obviously more complex with a strong coupling between the fluid and the structure.

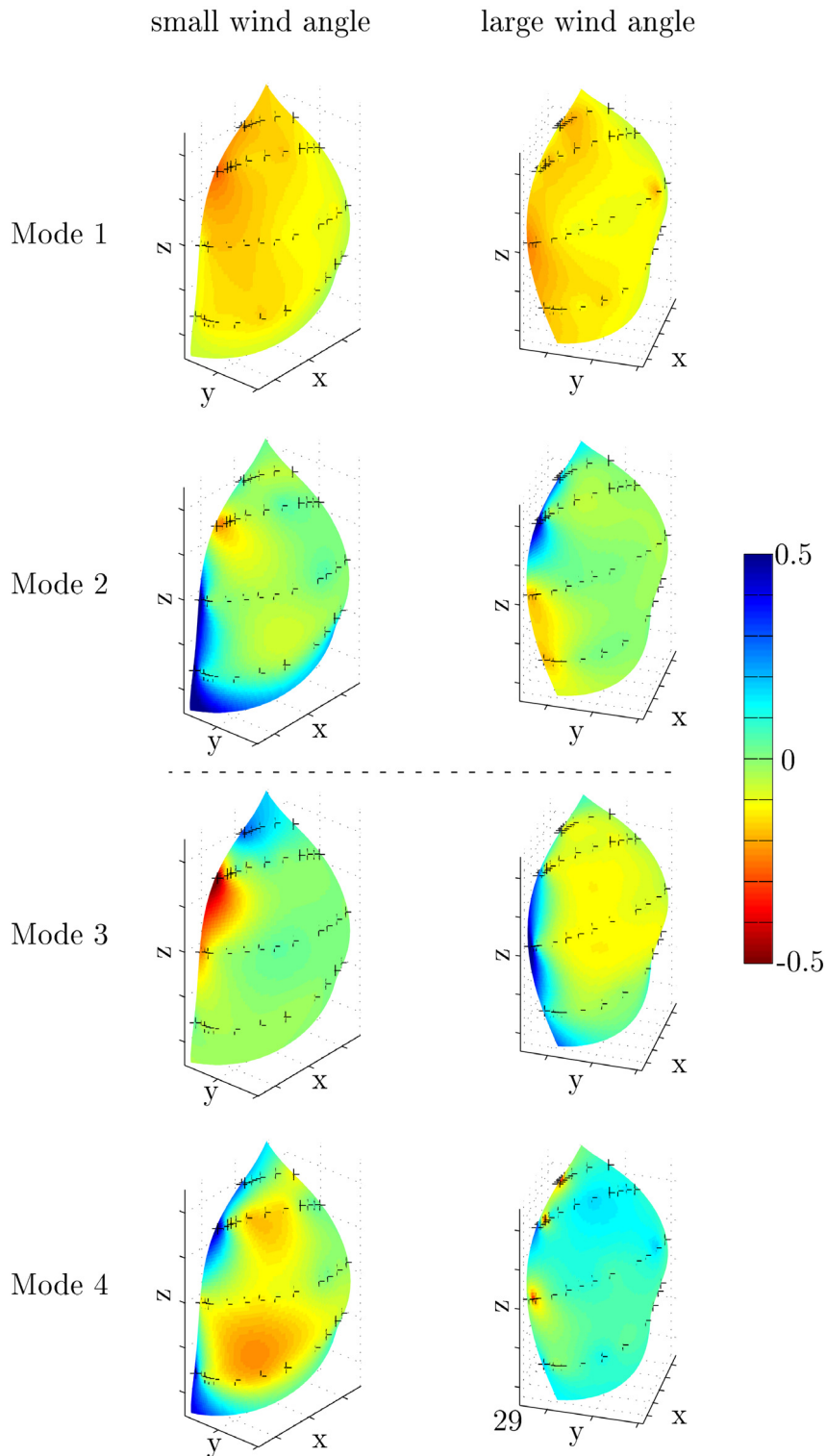


Fig. 8. Topos for small and large wind angles. Crosses represent the pressure taps. The color scale is arbitrary. The sail shape for each wind angle was measured by photogrammetry in a previous work (Deparday et al., 2016).

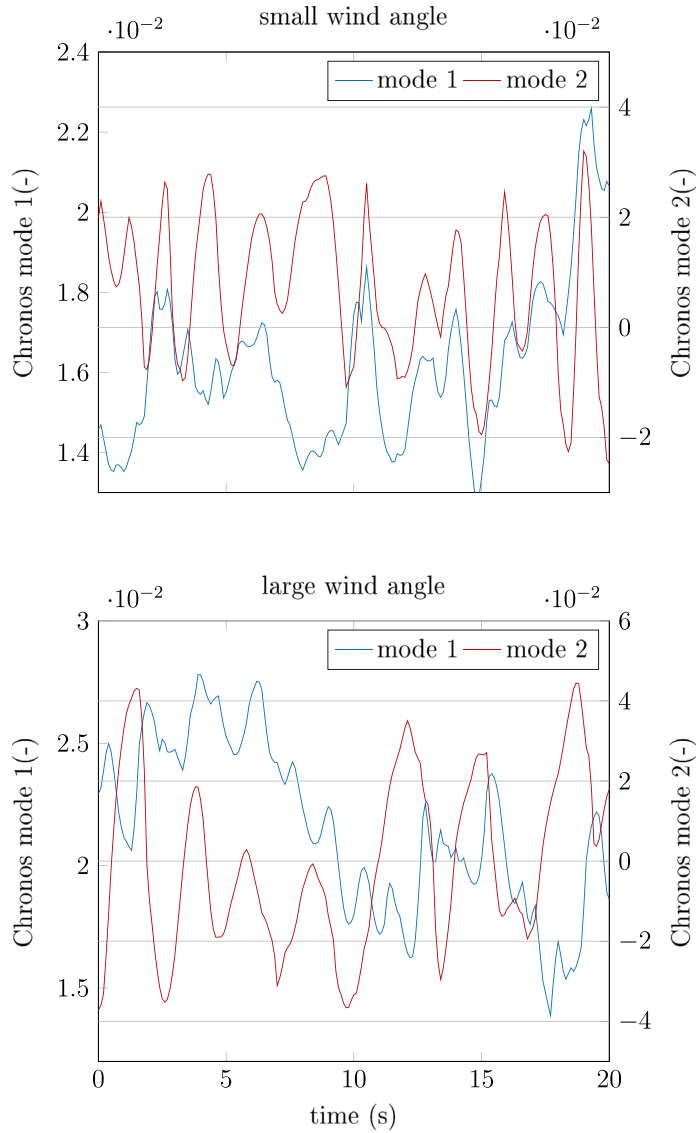


Fig. 9. Chronos of the pressures for two typical wind angles. Note the different scales for each mode.

5. Proposition of a physical mechanism of the flapping phenomenon

Based on the previous conclusions, a physical explanation of how this flapping phenomenon occurs is proposed. This physical interpretation takes inspiration in Connell and Yue (2007) with the description of the snapping event of a flag, where similarly there is a peak of tension during the strong acceleration which is associated with a shedding of strong vortices. For 2D membranes, Rojratsirikul et al. (2011) also present reduced frequencies similar to the ones found in the present work (see Table 1), confirmed by Bleischwitz et al. (2017). They suggest that the membrane vibrations might be coupled with the first harmonic of the natural vortex shedding frequency at high incidence.

We propose a physical interpretation of the flapping phenomenon which would require further validation. The four instants described in Section 3.2 (A, before the folding stage, B, at the beginning of folding, C at the maximum of folding and D after the unfolding stage) are used again to describe this physical explanation.

5.1. Membrane model

This physical interpretation is based on the membrane model with the general equation:

$$\rho_{surf} \frac{\partial^2 w}{\partial t^2} = \underline{\underline{\chi}} \underline{\underline{\kappa}} + \Delta P \quad (4)$$

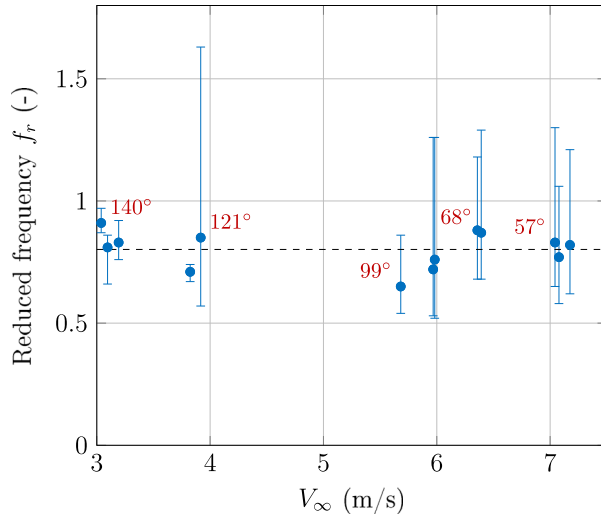


Fig. 10. Reduced frequency of the mode 2 chronos (blue dots) for different wind angles as a function of the wind speed. A fairly constant value is observed ≈ 0.8 . Symbols show the average and errorbars show the scattering (min and max) of the values determined over all oscillations in the run.

with:

w : normal displacement from plane (u, v)

ρ_{surf} : surface density of membrane

ΔP : difference of pressure

$\underline{\chi}$: tension tensor

$\underline{\kappa}$: curvature tensor: $-\frac{\partial^2 w}{\partial u \partial v} = -\nabla^2 w$.

As explained previously, this flapping phenomenon is 3 dimensional. There is a variation of pressure and shape along the flow and along the span. The curvature tensor can be estimated, as a first approach, by the mean curvature: $\nabla^2 w \approx \kappa_u + \kappa_v$. Near the leading edge, let us assume κ_u the principal curvature set streamwise, from the leading edge to the trailing edge, and κ_v , the principal curvature set spanwise, from the bottom to the top. On each string, Eq. (4) can be reduced to one dimension, with either u or v used depending on which string is considered:

$$\rho \frac{\partial^2 w}{\partial t^2} = T \frac{\partial^2 w}{\partial u^2} + F_{aero} \quad (5)$$

where F_{aero} is the integration of ΔP along the curve and T the linear tension. This equation explains that an increase of suction is counteracted by an increase of tension in the sail or an increase of curvature. For the same pressure distribution, a sail with more curvature should have less tension in the sailcloth. The curvature creates a bending stiffness.

5.2. Folding stage

Fig. 11 describes the physical interpretation during the folding stage. At instant A, the luff of the spinnaker stands still, hence $\frac{\partial^2 w}{\partial t^2} = 0$. ΔP as well as T are at a minimum. The sail is at a weak static equilibrium. Thwaites (1961) and Newman and Paidousis (1991) demonstrated that a loss of shape stability occurs for two-dimensional membranes held at both extremities, for a certain ratio between the camber, angle of attack and tension in the membrane. Furthermore, the leading edge of a spinnaker is only maintained in the spanwise direction by the tensions applied at the head and tack which set the sail (see Fig. 2) and might be even more subject to collapse. For a tension and a pressure suction small enough, the spinnaker starts folding (see Figs. 11(a) and 11(b)).

During the folding stage, from instant A to C, the spinnaker keeps folding, κ_u increases, and the pressure suction decreases because of a negative angle of attack. While the luff keeps folding, the shape of the profile changes and the leading edge shifts from the luff to a new leading edge further downstream. At instant C, the angle of attack of this “new” profile is larger (see Fig. 11(c)). When a flow encounters a thin profile with an angle of attack large enough, a leading edge vortex can be created (Viola et al., 2014; Bot et al., 2014 for sail applications). It creates a high suction area just after the folded area.

According to this description, before the creation of the high suction area, the more the leading edge folds, the lower the suction. The evolution of pressure up to instant C follows mostly the evolution of the folded area. The aerodynamic loads should be proportional to the amount of surface folded at the leading edge.

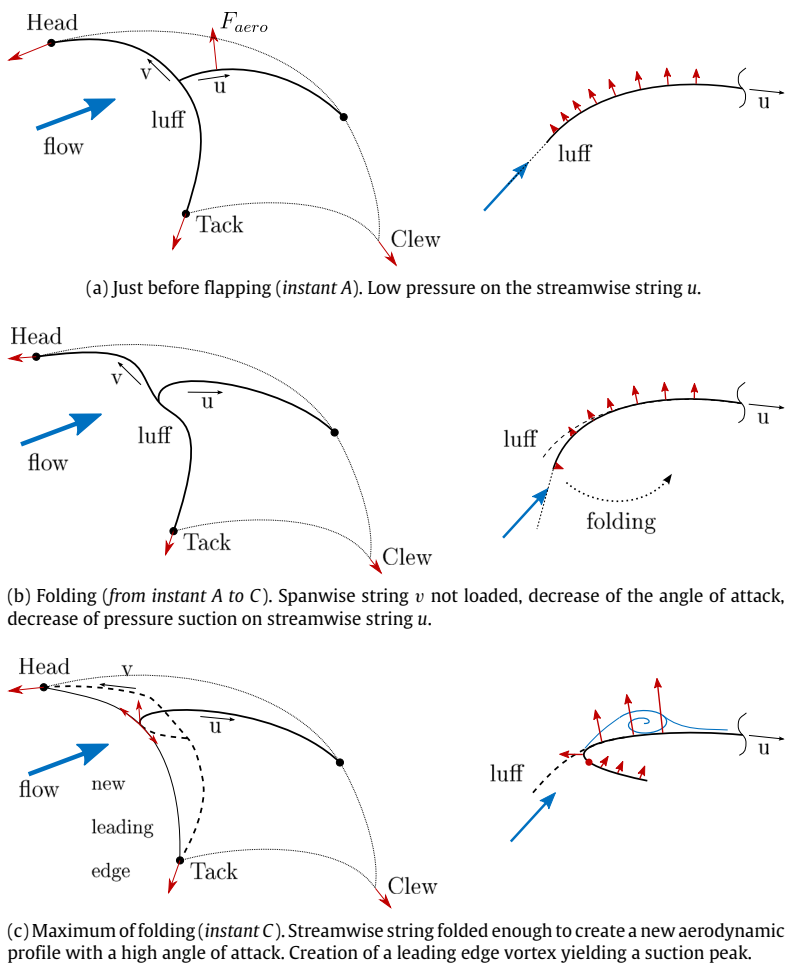


Fig. 11. *Folding stage.* Simplified representation of the spinnaker to model the flapping of the luff with one spanwise string v modeling the luff and one streamwise string u . Left: 3D perspective view; right: horizontal section.

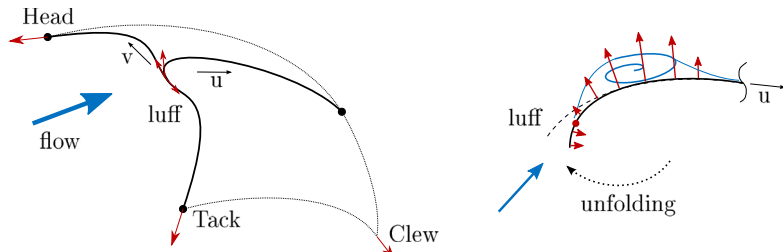
5.3. Unfolding stage

In the folded area, the tension is low because the sail has more curvature and less pressure. Downstream the new leading edge, the high suction yields a high tension in the sail. There is therefore a difference of tension at the frontier of the folded area (see red arrows on the 2-string models in Fig. 12). The tension is spread spanwise and towards the high suction area, further downstream. This difference of tension tends to pull the folded area and therefore to unfold the luff. Moreover, the stagnation point (represented by a red point in Fig. 11(c)) is upstream the limit of the folded area. At this point, the pressure is null. Therefore, a small part of the folded area – the most curved part – has a high suction which tends to unfold the sail too.

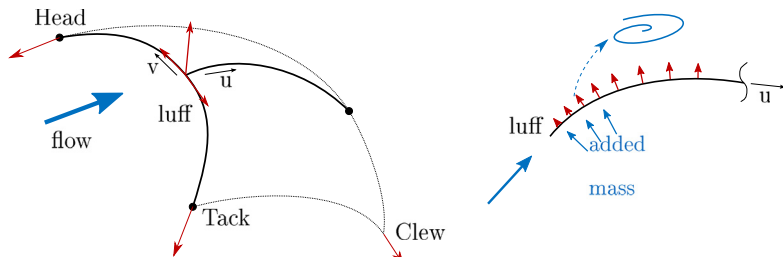
During the unfolding stage (from instant C to D), the leading edge vortex expands (see Fig. 12(a)). The tension at the limit of the folded area increases and contributes also to unfold the luff up to the full recovery of the flying shape (instant D).

At instant D, the spinnaker is unfolded. Just before that instant, a strong deceleration abruptly stops the unfolding motion. The spanwise tension and curvature prevent the spinnaker from being folded streamwise in the other direction. During the folding, the spanwise tension and curvature are null because the v string is slack. But as soon as the spinnaker recovers its full flying shape, the high suction at the leading edge suddenly tensions the luff (see Fig. 12(b)). During this sudden deceleration, the inertia of the air displaced on the windward side by the movement of the luff (the added mass) adds an extra tension in the luff. On the leeward side, the leading edge vortex is torn away from the luff by the air added mass when the unfolding is stopped, and the vortex is shed. Then, the pressure is low again, and after this high peak of tension, the situation gets back to the state of instant A and the process can start again. Hence, a periodic flapping can settle in the absence of any external periodic forcing.

Similar to the folding stage, the aerodynamic load varies with the size of the folding of the leading edge. But contrary to the folding stage, there is a fast formation and vanishing of a suction area. The unfolding stage (C to D) is short in time (two



(a) Unfolding (from instant C to D). Due to high gradient of pressure at the luff, streamwise string unfolds. Leading edge vortex expands.



(b) Full flying shape again (instant D). Spanwise string suddenly tensioned, stopping abruptly the unfolding of the streamwise string. Peak of load due to displaced air around the luff. Leading edge vortex is detached and shed, low pressure suction back on the streamwise string. The situation is back to state A (11(a)).

Fig. 12. Unfolding stage. Simplified representation of the spinnaker to model the flapping of the luff with one spanwise string v modeling the luff and one streamwise string u . Left: 3D perspective view; right: horizontal section.

times faster than the folding stage) with a large displacement of the sail. Then, the accelerations of the structure might be of first order and hence the added mass of the fluid might contribute the most to the variations of loads. When the unfolding stage starts, a variation of slope in the loads is indeed noticed in Fig. 4.

5.4. 3D aspect of the flapping instability

The previous interpretation describes the flapping in a horizontal section at one height only and the reality is of course a more complex 3D phenomenon. The leading edge vortex stays attached in the top part of the spinnaker where the full shape is recovered, “locked” by the expansion of the leading edge vortex in the folded middle part. When the flapping finishes, the high suction is disappearing on the whole span of the sail.

The fold of the leading edge at a certain height of the span tends to change the angle of attack along the span, similar to torsion on wings. Therefore, next to the folded area, there is a higher suction at the leading edge (above or below the folded area depending on the wind angle) due to the larger angle of attack maintained.

To obtain the most efficient flapping (meaning optimizing the time-averaged total aerodynamic force generated during the flapping phenomenon), the fold of the leading edge should be as little as possible (to minimize the low suction area) and should also affect as much as possible the whole span by increasing the high suction area.

6. Conclusions

A fluid–structure interaction instability of a light, soft and highly cambered membrane is described based on in-situ experimental data. A yacht downwind sail – a spinnaker – is characterized by an instability which is a periodic flapping of the free leading edge. It differs from the fluid–structure interaction instabilities commonly found in the literature because of the highly cambered soft membrane only held at 3 points, the very low flexural rigidity and structure mass, and a high Reynolds number. Development of a dedicated onboard instrumentation allows to simultaneously measure loads, shape and pressure distribution.

The Bi-Orthogonal Decomposition (BOD) applied to the pressure fields proves its ability to extract the essential dynamics of this complex aeroelastic problem. The global aerodynamic force is mostly represented by mode 1 – which might be called *the aerodynamic mode* – while mode 2 mostly represents the effects of the membrane flapping – and might be called *a structural mode*. A constant reduced frequency of the flapping is found and is associated with a variation of pressure at the leading edge.

The discussion of the space and time evolution of pressures and shapes analyzed during the periodic folding and unfolding of the leading edge suggests that the creation and shedding of a leading edge vortex might play a key role in this instability.

Further investigation should be done to ascertain the cause of this instability. With a better understanding of this aeroelastic problem, it might be possible to better understand how the variation of pressures due to flapping helps to increase the time-average propulsive load.

Acknowledgments

This project has received funding from the European Union's Seventh Programme for research, technological development and demonstration under grant agreement No PIRSES-GA-2012-318924, and from the Royal Society of New Zealand for the UK-France-NZ collaboration project SAILING FLUIDS. These experiments were made possible thanks to the IRENAV's technical staff (SCEFER). The authors would also gratefully thank Frédéric Hauville for all the work he did on these experiments as well as Marc Rabaud and Pascal Hémon for all the fruitful discussions.

References

- Alben, S., 2008. The flapping-flag instability as a nonlinear eigenvalue problem. *Phys. Fluids* 20 (10), 104106.**
- Aubin, N., Augier, B., Deparday, J., Sacher, M., 2017. To curl or not to curl: Wind tunnel investigations of spinnaker performance. In: The 4th International Conference on Innovation in High Performance Sailing Yachts, Lorient.
- Aubin, N., Augier, B., Deparday, J., Sacher, M., Bot, P., 2018. Performance enhancement of downwind sails due to leading edge flapping: a wind tunnel investigation. *Ocean Eng.* (submitted for publication).
- Aubry, N., Guyonnet, R., Lima, R., 1991. Spatiotemporal analysis of complex signals: theory and applications. *J. Stat. Phys.* 64 (3–4), 683–739.
- Augier, B., Bot, P., Hauville, F., Durand, M., 2012. Experimental validation of unsteady models for fluid structure interaction: Application to yacht sails and rigs. *J. Wind Eng. Ind. Aerodyn.* 101, 53–66.
- Augier, B., Bot, P., Hauville, F., Durand, M., 2013. Dynamic behaviour of a flexible yacht sail plan. *Ocean Eng.* 66, 32–43.
- Augier, B., Hauville, F., Bot, P., Aubin, N., Durand, M., 2014a. Numerical study of a flexible sail plan submitted to pitching: Hysteresis phenomenon and effect of rig adjustments. *Ocean Eng.* 90, 119–128.
- Augier, B., Yan, J., Korobenko, A., Czarnowski, J., Ketterman, G., Bazilevs, Y., 2014b. Experimental and numerical FSI study of compliant hydrofoils. *Comput. Mech.* 55 (6), 1079–1090.
- Bergmann, M., Iollo, A., 2011. Modeling and simulation of fish-like swimming. *J. Comput. Phys.* 230 (2), 329–348.
- Bleischwitz, R., de Kat, R., Ganapathisubramani, B., 2017. On the fluid-structure interaction of flexible membrane wings for MAVs in and out of ground-effect. *J. Fluids Struct.* 70, 214–234.
- Bot, P., Viola, I.M., Flay, R.G., Brett, J.S., 2014. Wind-tunnel pressure measurements on model-scale rigid downwind sails. *Ocean Eng.* 90, 84–92.
- Campbell, I.M.C., 2014. A comparison of downwind sail coefficients from tests in different wind tunnels. *Ocean Eng.* 90, 62–71.
- Chae, E.J., Akcabay, D.T., Lelong, A., Astolfi, J.A., Young, Y.L., 2016. Numerical and experimental investigation of natural flow-induced vibrations of flexible hydrofoils. *Phys. Fluids* 28 (7), 075102.
- Combes, S. a., Daniel, T.L., 2001. Shape, flapping and flexion: wing and fin design for forward flight. *J. Exp. Biol.* 204 (Pt 12), 2073–2085.
- Connell, B.S.H., Yue, D.K.P., 2007. Flapping dynamics of a flag in a uniform stream. *J. Fluid Mech.* 581, 33–67.
- Daniel, T.L., Combes, S.A., 2002. Flexible wings and fins: bending by inertial or fluid-dynamic forces? *Integr. Comp. Biol.* 42 (5), 1044–1049.
- Deparday, J., 2016. Experimental Studies of Fluid-Structure Interaction on Downwind Sails (Ph.D. thesis), IRENAV, UBO, p. 230.
- Deparday, J., Bot, P., Hauville, F., Augier, B., Rabaud, M., 2016. Full-scale flying shape measurement of offwind yacht sails with photogrammetry. *Ocean Eng.* 127 (November 2016), 135–143.
- Deparday, J., Bot, P., Hauville, F., Motta, D., Le Pelley, D.J., Flay, R.G., 2014. Dynamic measurements of pressures, sail shape and forces on a full-scale spinnaker. In: The 23rd HISWA Symposium on Yacht Design and Yacht Construction. Presented in Amsterdam, pp. 61–73.
- Durand, M., Leroyer, A., Lothodé, C., Hauville, F., Visonneau, M., Floch, R., Guillaume, L., 2014. FSI investigation on stability of downwind sails with an automatic dynamic trimming. *Ocean Eng.* 90 (2013), 129–139.
- Eloy, C., Kofman, N., Schouwiler, L., 2011. The origin of hysteresis in the flag instability. *J. Fluid Mech.* 691, 583–593.
- Fish, F.E., 1999. Performance constraints on the maneuverability of flexible and rigid biological systems. In: Proceedings of the Eleventh International Symposium on Unmanned Untethered Submersible Technology. Autonomous Undersea Systems Institute, Durham New Hampshire, pp. 394–406.
- Flay, R.G., 1996. A twisted flow wind tunnel for testing yacht sails. *J. Wind Eng. Ind. Aerodyn.* 63 (1–3), 171–182.
- Fossati, F., Bayati, I., Orlandini, F., Muggiasca, S., Vandone, A., Mainetti, G., Sala, R., Bertorello, C., Begovic, E., 2015. A novel full scale laboratory for yacht engineering research. *Ocean Eng.* 104, 219–237.
- Fossati, F., Muggiasca, S., 2011. Experimental investigation of sail aerodynamic behavior in dynamic conditions. *J. Sailboat Technol.* 2 (03), 1–42.
- Garrett, R., 1987. The Symmetry of Sailing. Adlard Coles, London, p. 268.
- Gerhardt, F.C., Flay, R.G., Richards, P.J., 2011. Unsteady aerodynamics of two interacting yacht sails in two-dimensional potential flow. *J. Fluid Mech.* 668, 551–581.
- Glück, M., Breuer, M., Durst, F., Halfmann, A., Rank, E., 2001. Computation of fluid-structure interaction on lightweight structures. *J. Wind Eng. Ind. Aerodyn.* 89 (14–15), 1351–1368.
- Graf, K., Müller, O., 2009. Photogrammetric investigation of the flying shape of spinnakers in a twisted flow wind tunnel. In: The 19th Chesapeake Sailing Yacht Symposium, Annapolis.
- Heathcote, S., Wang, Z., Gursul, I., 2008. Effect of spanwise flexibility on flapping wing propulsion. *J. Fluids Struct.* 24 (2), 183–199.
- Hémon, P., Santi, F., 2003. Applications of biorthogonal decompositions in fluidstructure interactions. *J. Fluids Struct.* 17 (8), 1123–1143.
- Herman, J.S., 1989. A Sail Force Dynamometer: Design, Implementation and Data Handling (Ph.D. thesis), Massachussets Institute of Technology, p. 52.
- Hochkirch, K., Brandt, H., 1999. Fullscale hydrodynamic force measurement on the Berlin sailing dynamometer. In: 14th Chesapeake Sailing Yacht Symposium, Annapolis, pp. 33–44.
- Huang, L., 1995. Flutter of cantilevered plates in axial flow. *J. Fluids Struct.* 9 (2), 127–147.
- Khalak, A., Williamson, C., 1996. Dynamics of a hydroelastic cylinder with very low mass and damping. *J. Fluids Struct.* 10 (5), 455–472.
- Khalak, A., Williamson, C., 1999. Motions, forces and mode transitions in vortex-induced vibrations at low mass-damping. *J. Fluids Struct.* 13 (7–8), 813–851.
- Knight, J.J., Lucey, A.D., Shaw, C.T., 2010. Fluid-structure interaction of a two-dimensional membrane in a flow with a pressure gradient with application to convertible car roofs. *J. Wind Eng. Ind. Aerodyn.* 98 (2), 65–72.

- Le Pelley, D.J., Morris, D., Richards, P., 2012. Aerodynamic force deduction on yacht sails using pressure and shape measurements in real time. In: 4th High Performance Yacht Design Conference, Auckland.
- Le Pelley, D.J., Richards, P.J., Berthier, A., 2015. Development of a directional load cell to measure flying sail aerodynamic loads. In: 5th High Performance Yacht Design Conference, Auckland, pp. 66–75.
- Lemaitre, C., Hémon, P., de Langre, E., 2005. Instability of a long ribbon hanging in axial air flow. *J. Fluids Struct.* 20 (7 Spec. Iss.), 913–925.
- Leroyer, A., Visonneau, M., 2005. Numerical methods for RANSE simulations of a self-propelled fish-like body. *J. Fluids Struct.* 20 (7), 975–991.
- Lozej, M., Golob, D., Bokal, D., 2012. Pressure distribution on sail surfaces in real sailing conditions. In: The 4th High Performance Yacht Design Conference, Auckland, pp. 242–251.
- Marais, C., Thiria, B., Wesfreid, J.E., Godoy-Diana, R., 2012. Stabilizing effect of flexibility in the wake of a flapping foil. *J. Fluid Mech.* 710 (September), 659–669.
- Marchaj, C.A., 1962. Sailing Theory and Practice. Adlard Coles.
- Masuyama, Y., 2014. The work achieved with the sail dynamometer boat "fujin", and the role of full scale tests as the bridge between model tests and CFD. *Ocean Eng.* 90, 72–83.
- Miao, J.M., Ho, M.H., 2006. Effect of flexure on aerodynamic propulsive efficiency of flapping flexible airfoil. *J. Fluids Struct.* 22 (3), 401–419.
- Michalski, A., Gawenat, B., Gelenne, P., Haug, E., 2015. Computational wind engineering of large umbrella structures. *J. Wind Eng. Ind. Aerodyn.* 144, 96–107.
- Michelin, S., Llewellyn Smith, S.G., 2009a. Linear stability analysis of coupled parallel flexible plates in an axial flow. *J. Fluids Struct.* 25 (7), 1136–1157.
- Michelin, S., Llewellyn Smith, S.G., 2009b. Resonance and propulsion performance of a heaving flexible wing. *Phys. Fluids* 21 (7).
- Motta, D., Flay, R., Richards, P., Le Pelley, D., Bot, P., Deparday, J., 2015. An investigation of the dynamic behaviour of asymmetric spinnakers at full-scale. In: 5th High Performance Yacht Design Conference, pp. 76–85.
- Motta, D., Flay, R.G.J., Richards, P.J., Pelley, D.J.L., Deparday, J., Bot, P., 2014. Experimental investigation of asymmetric spinnaker aerodynamics using pressure and sail shape measurements. *Ocean Eng.* 90, 104–118.
- Mountcastle, A.M., Daniel, T.L., 2009. Aerodynamic and functional consequences of wing compliance. *Exp. Fluids* 46 (5), 873–882.
- Murua, J., Palacios, R., Peiró, J., 2010. Camber effects in the dynamic aeroelasticity of compliant airfoils. *J. Fluids Struct.* 26 (4), 527–543.
- Newman, B., Paidousis, M., 1991. The stability of two-dimensional membranes in streaming flow. *J. Fluids Struct.* 00, 443–454.
- Paidousis, M.P., 2004. Fluid-Structure Interactions: Slender Structures and Axial Flow. Elsevier, p. 1040.
- Rojratsirikul, P., Genc, M., Wang, Z., Gursul, I., 2011. Flow-induced vibrations of low aspect ratio rectangular membrane wings. *J. Fluids Struct.* 27 (8), 1296–1309.
- Schouveiler, L., Eloy, C., 2009. Coupled flutter of parallel plates. *Phys. Fluids* 21 (8).
- Schouveiler, L., Hover, F.S., Triantafyllou, M.S., 2005. Performance of flapping foil propulsion. *J. Fluids Struct.* 20, 949–959.
- Shyy, W., Aono, H., Chimakurthi, S., Trizila, P., Kang, C.-K., Cesnik, C., Liu, H., 2010. Recent progress in flapping wing aerodynamics and aeroelasticity. *Prog. Aerosp. Sci.* 46 (7), 284–327.
- Takizawa, K., Kostov, N., Puntel, A., Henicke, B., Tezduyar, T.E., 2012. Space-time computational analysis of bio-inspired flapping-wing aerodynamics of a micro aerial vehicle. *Comput. Mech.* 50 (6), 761–778.
- Takizawa, K., Tezduyar, T.E., Kostov, N., 2014. Sequentially-coupled space-time FSI analysis of bio-inspired flapping-wing aerodynamics of an MAV. *Comput. Mech.* 54 (2), 213–233.
- Thwaites, B., 1961. The aerodynamic theory of sails. I. Two-dimensional sails. *Proc. R. Soc. Lond. Ser. A Math. Phys. Eng. Sci.* 261 (1306), 402–422.
- Tiomkin, S., Raveh, D.E., 2017. On the stability of two-dimensional membrane wings. *J. Fluids Struct.* 71, 143–163.
- Viola, I.M., Bartesaghi, S., Van-Renterghem, T., Ponzini, R., 2014. Detached Eddy simulation of a sailing yacht. *Ocean Eng.* 90 (November 2014), 93–103.
- Viola, I.M., Bot, P., Riotti, M., 2013. Upwind sail aerodynamics: A RANS numerical investigation validated with wind tunnel pressure measurements. *Int. J. Heat Fluid Flow* 39, 90–101.
- Viola, I.M., Flay, R.G., 2009. Force and pressure investigation of modern asymmetric spinnakers. *Trans. R. Inst. Nav. Archit. B* 151 (2), 31–40.
- Viola, I.M., Flay, R.G., 2010. Full-scale pressure measurements on a Sparkman and Stephens 24-foot sailing yacht. *J. Wind Eng. Ind. Aerodyn.* 98 (12), 800–807.
- Viola, I.M., Flay, R.G., 2011. Sail pressures from full-scale, wind-tunnel and numerical investigations. *Ocean Eng.* 38 (16), 1733–1743.
- Waldman, R.M., Breuer, K.S., 2017. Camber and aerodynamic performance of compliant membrane wings. *J. Fluids Struct.* 68 (November 2016), 390–402.
- Watanabe, Y., Suzuki, S., Sugihara, M., Sueoka, Y., 2002. An experimental study of paper flutter. *J. Fluids Struct.* 16 (4), 529–542.
- Williamson, C.H.K., 1996. Vortex dynamics in the cylinder wake. *Annu. Rev. Fluid Mech.* 28 (1), 477–539.
- Wood, R., 2007. Liftoff of a 60 mg flapping-wing MAV. In: IEEE International Conference on Intelligent Robots and Systems, pp. 1889–1894.
- Yan, J., Augier, B., Korobenko, A., Czarnowski, J., Ketterman, G., Bazilevs, Y., 2015. FSI modeling of a propulsion system based on compliant hydrofoils in a tandem configuration. *Comput. & Fluids* 141, 201–211.
- Zhang, Z., Wrist, A., Hubner, J.P., 2017. Effects of leading-edge vibration on a spanwise-tensioned membrane at low Reynolds number. *J. Fluids Struct.* 69 (December 2016), 441–457.
- Zhu, L., Peskin, C.S., 2002. Simulation of a flapping flexible filament in a flowing soap film by the immersed boundary method. *J. Comput. Phys.* 179 (2), 452–468.